How to cite: *Angew. Chem. Int. Ed.* **2023,** *62,* e202216776
International Edition: doi.org/10.1002/anie.202216776
German Edition: doi.org/10.1002/ange.202216776

Perovskites | Hot Paper

Identifying the Interfacial Polarization in Non-stoichiometric Lead-Free Perovskites by Defect Engineering

Ze Xu, Yi-Xuan Liu, Maryam Azadeh, Hao-Cheng Thong, Yuqi Jiang, Fang-Zhou Yao, Zhen-Xing Yue, Zhong-Tai Zhang, Zi-Long Tang, Jing-Feng Li, Heng Wang, Till Frömling,* and Ke Wang**

Abstract: Recent advances in perovskite ferroelectrics have fostered a host of exciting sensors and actuators. Defect engineering provides critical control of the performance of ferroelectric materials, especially lead-free ones. However, it remains a challenge to quantitatively study the concentration of defects due to the complexity of measurement techniques. Here, a feasible approach to analyzing the A-site defect and electron in alkali metal niobate is demonstrated. The theoretical relationships among defect concentration, conductivity, and oxygen partial pressure can be established based on the defect chemistry equilibria. The type and concentration of defects are reflected through the conductivity variation with oxygen partial pressure. As a result, the variation of defect concentration gives rise to defect-driven interfacial polarization, which further leads to distinct properties of the ceramics. e.g., abnormal dielectric behavior. Furthermore, this study also suggests a strategy to manipulate defects and charges in perovskite oxides for performance optimization.

[*] Z. Xu, Y.-X. Liu, H.-C. Thong, Y. Jiang, F.-Z. Yao, Z.-X. Yue, Z.-T. Zhang, Z.-L. Tang, J.-F. Li, K. Wang
State Key Laboratory of New Ceramics and Fine Processing, School of Materials Science and Engineering, Tsinghua University
Beijing 100084 (P. R. China)
E-mail: wang-ke@tsinghua.edu.cn

M. Azadeh, T. Frömling
Institute of Materials Science,
Technische Universität Darmstadt
64287 Darmstadt (Germany)
E-mail: froemling@ceramics.tu-darmstadt.de

H. Wang
Department of Mechanical, Materials and Aerospace Engineering, Illinois Institute of Technology
Chicago, IL 60616 (USA)
E-mail: heng.wang@iit.edu

Introduction

Perovskites are widely used in cutting-edge electronic devices, including photovoltaics,[1] optoelectronics,[2] and piezoelectrics. Ferroelectric perovskites belong to the most important ferroelectrics because of their favorable characteristics, i.e., spontaneous polarization and domain switchability.[3] Defect engineering has been a powerful approach for modulating the properties of perovskite materials,[4] including ferroelectric perovskites.[5] For instance, defect engineering has been frequently employed to lead zirconate titanate (PZT) to produce high piezoelectricity and low mechanical and dielectric losses.[6] A-site deficiency in alkali metal niobate, e.g., sodium niobate and potassium sodium niobate (KNN),[7] can form local heterogeneity and thus giant piezoelectricity. In addition, oxygen vacancies can greatly improve the electrical transducer efficiency of many ferroelectric materials because of their hardening effect.[6c,8] Therefore, an in-depth understanding of the nature of defect formation and its impact on the properties of materials is the key to promoting the flexibility of defect engineering.

Some defects (A-site vacancies or oxygen vacancies) can intrinsically form in ferroelectric perovskites, including PZT, KNN, and sodium bismuth titanate (BNT), during the sintering process because of the volatilization of A-site elements.[9] Technically, controlling performance through manipulating the defect concentration is not straightforward. Due to the electroneutrality condition, introducing a charged defect always creates an additional oppositely charged defect.[9a] Another problem is that the quantitative analysis of defects in ferroelectrics is still challenging where electrical properties are sensitive to the defect concentration. Thus, developing methods for quantitatively characterizing defects is an important research topic in defect engineering. Numerous techniques are available to obtain the qualitative information, e.g., radio spectroscopy (i.e., electron spin resonance (ESR) and nuclear magnetic resonance (NMR)),[10] positron annihilation lifetime spectroscopy (PALS),[11] impedance spectroscopy,[6a,12] X-ray photoelectron spectroscopy (XPS), photoluminescence[13] and transmission electron microscope (TEM).[9a] These characterizations are frequently used to study the defects in ferroelectric perovskites. Among these approaches, XPS, UV/Vis, ESR, NMR, and PALS are often used to analyze defects, such as oxygen defects, and polyvalent ion defects

(e.g., Mn ion defects, Fe ion defects, etc.). However, they can only be used for qualitative analysis and are applicable to limited types of defects.[14] Impedance spectroscopy is an indirect measurement approach and is often used in defect analysis of PZT, BNT, and barium titanate,[12] which is also a qualitative method.[6a] TEM can directly observe the defects but the irradiation of a high-energy electron beam could potentially damage the sample and introduce artefacts.[7a,b,15] The stringent requirements of thickness and orientation of samples further limit its application to microanalysis at the nanoscale.[16] In quantitative microanalysis, a universal problem is how to obtain reliable and accurate results under the condition of small geometric changes.[17] So far, it is still difficult to analyze the profound impact of defects for the lack of an effective and universal macro defect analysis method.

KNN and BNT, are promising environmentally-benign candidates for piezoelectrics to replace the hazardous PZT. Interestingly, the mature defect engineering approach successfully applied to PZT fails in the KNN and BNT systems, especially A-site defects. A-site defects are supposed to increase domain wall mobility through softening effect in PZT-based ceramics and further promote the piezoelectric response of the material.[18] A-site defects can change the stress conditions of the BNT-based ceramics, inducing a structure with enlarged interplanar spacing.[19] Similar results have also been reported in KNN systems, with Wang reporting an enhanced d_{33} of 324 pC/N through A-site element doping and Liu announcing a thermostable d_{33}* of 320 pm/V through intrinsic defect engineering recently.[20] Liu and Wu further presented that the local heterogeneity introduced by A-site defects in niobium-based perovskites could significantly boost the piezoelectric performance of these materials.[7a,b] Undoubtedly, the performance of ferroelectrics can be further optimized with a better understanding of in-depth analysis of A-site defects. For BNT, it could nevertheless be revealed that a complex interaction of defect couples is responsible for the deviation from the expected behaviors.[21] However, the current understanding of the influence of defects in niobium-based ferroelectric perovskites is far from satisfactory. Many phenomena in KNN are still not well understood, such as conductivity mechanism, narrow sintering window, abnormal dielectric behavior, and poor stability.[22] Investigation of defects in KNN is meaningful to fundamental scientific research and beneficial to industrial development. In the present study, we propose a feasible approach to evaluate the intrinsic defect in the KNN bulk sample and then analyze defect-driven polarization that affects the dielectric behavior of materials. Prototypical KNN with different compositions, i.e., $(Na_{0.52}K_{0.48})NbO_3$ (i.e., KNN) and stoichiometric Na-excess $(Na_{0.535}K_{0.48})NbO_3$ (denoted as KNN-Na), prepared by hot pressing are systematically investigated. First, a theoretical defect chemistry concentration as a function of oxygen partial pressure (denoted as the Brouwer diagram) is provided, which serves as a good reference for the semi-quantitatively determination of dominating defect types and their concentrations. The impedance spectra of KNN and KNN-Na are then compared based on their Brouwer diagram, suggesting the n-type conducting mechanism in these materials. Moreover, we show that such an understanding of defect chemistry is sufficient for analyzing some defect-related experimental phenomena in KNN, e.g., dielectric anomalies. This paper investigates the effect of defect concentrations on the polarization of ferroelectric perovskites, suggesting a new concept and method for understanding the polarization mechanism of ferroelectricity from the perspective of defects.

Results and Discussion

Theoretical analysis of defect chemistry. By solving a combination of defect equilibria with a reduced electroneutrality condition, we can evaluate the defect chemistry diagram of ABO_3 as a function of oxygen partial pressure (pO_2), as shown in the Brouwer diagram in Figure 1a,[23] and Supporting Information Note. In this model, the chemical valence of A is assumed to be 1, and B is considered not volatile. Generally, the Brouwer diagram can be classified into three sections with respect to the reduced electroneutrality conduction, i.e., low (range I), medium (II), and high pO_2 (range III).[24] Since conductivity is linearly proportional to the defect concentration when the temperature is stable, it is reasonable to measure the conductivity to infer the dominating defect type concerning the conductivity, see Supporting Information Note. For example, a negative slope of $-1/4$ in range II would indicate that electrons are the dominant charge carriers.

The Brouwer approximation of the electroneutrality condition does not precisely describe the actual behavior during the transition between different ranges. The relationship between defect concentration and pO_2 is no longer linear, as shown in Figure 1a inset. In addition, mixed conductance is often observed due to the presence of electronic and ionic charge carriers. Based on Figure 1a, the prediction of conductivity as a function of pO_2 can be constructed, which is Figure 1b. Assuming that two ABO_3: $A_{1-x}BO_{3-y}$ and $A_{1-2x}BO_{3-z}$ (x is the A-site vacancy concentration. y and z are oxygen vacancies concentration), where A-site vacancies are low ($A_{1-x}BO_{3-y}$) and high ($A_{1-2x}BO_{3-z}$), respectively. The difference in stoichiometry leads to different starting defect chemistry and hence different behavior towards pO_2. $A_{1-x}BO_{3-z}$ is donor doped compared to $A_{1-2x}BO_{3-z}$, leading to the shift to the right, as shown in Figure 1c. k_1 is the conductivity slope of $A_{1-x}BO_{3-y}$ in high pO_2. k_2 is the conductivity slope of $A_{1-2x}BO_{3-z}$ in low pO_2. k_3 is the conductivity slope of $A_{1-x}BO_{3-y}$ in low pO_2. It can be found that $|k_1| = |k_2| < |k_3|$. Thus, we can compare their conductivity slopes for two ABO_3 with different A-site defect concentrations to judge the difference in their defect concentrations. The electron concentration of $A_{1-x}BO_{3-y}$ (k_3) is obviously higher than that of $A_{1-2x}BO_{3-z}$ (k_2).

Application of the defect chemistry in KNN. A-site defects are common in KNN materials due to the volatilization of alkali metals, which is the reason for their large variation of performance. Herein, we designed two ceramics,

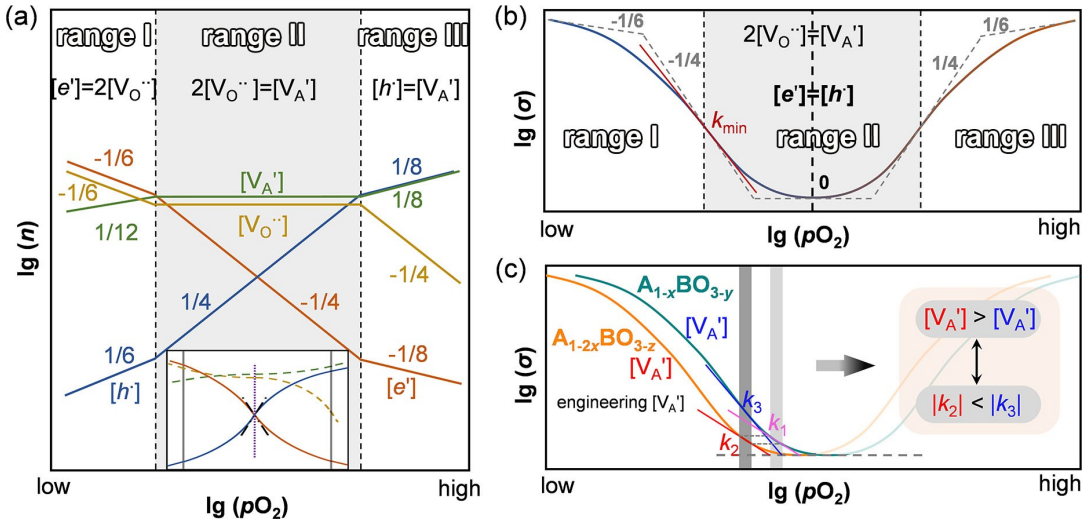

Figure 1. Brouwer diagrams in ABO_3 (the chemical valence of A is 1 and B is not volatile) and its application method. a) Theoretical relationship between defect concentration and pO_2 with the Brouwer approximation. The inset illustrates the actual functional relationship. b) Prediction of conductivity as a function of pO_2, when the change of conductance depends mainly on electrons and holes. k_{min} is the minimum value of the slope, which is larger than $-1/4$. c) The relationship between conductivity and pO_2 under different A-site vacancy concentrations. The change of A-site vacancy concentration causes the shift of the curve. k_1, k_2 and k_3 are the slope for $A_{1-x}BO_{3-y}$ at high pO_2, $A_{1-2x}BO_{3-z}$ at low pO_2, and $A_{1-x}BO_{3-y}$ at low pO_2.

KNN and KNN-Na. The impedance spectra are measured at 700 °C at a medium pO_2, as shown in Figure 2a and b. Conductivities are calculated from the impedance spectra measured as a function of pO_2 and summarized in Figure 2c. Linear fitting is performed for both data groups, which results in a good fit, as shown in Table S1. Negative slopes of −0.19 and −0.22 are obtained for KNN and KNN-Na. The negative slopes close to −0.25 suggest that the electron is the dominating conducting mechanism. The slope difference between KNN and KNN-Na agrees well with the expected trend from the defect chemistry diagram. In range II, the conductivity will be affected by the higher ionic conductivity of KNN, but the slope will be almost unaffected, as shown in Figure S1. The more negative slope in KNN-Na can be seen as a result of more electrons and fewer A-site vacancies, as illustrated in Figure 1c. The molar ratio of the three elements is determined by ICP tests of K, Na, and Nb elements, as shown in Figure 2d. The actual

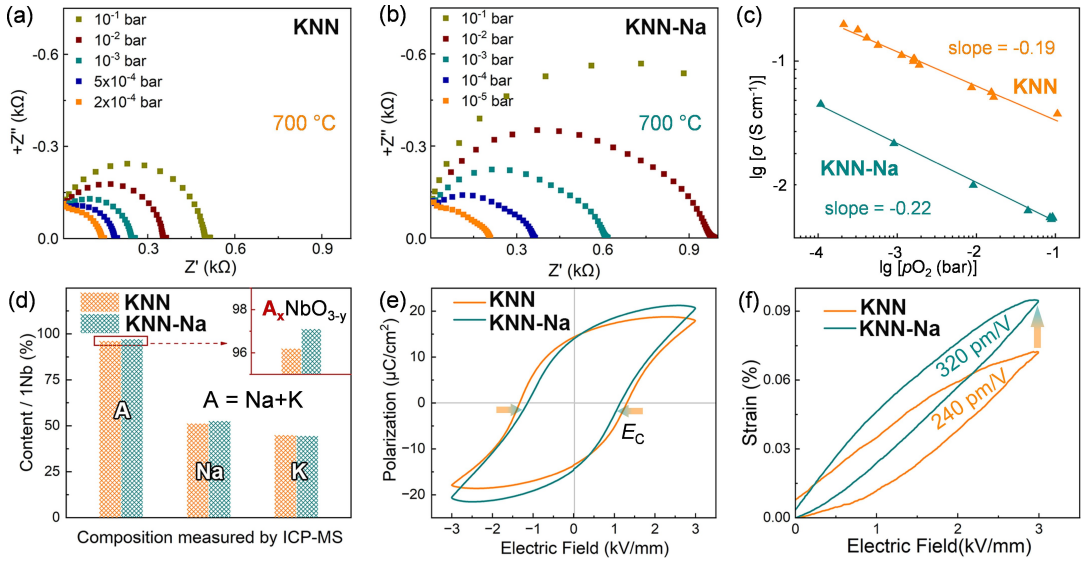

Figure 2. Comprehensive properties of KNN and KNN-Na. Complex impedance plots for a) KNN and b) KNN-Na at different pO_2 ($pO_2 = 10^{-1}$ to 10^{-4} bar at 700 °C), c) lg σ as a function of lg (pO_2) for KNN and KNN-Na, d) A-site content corresponding to unit Nb atom by inductively coupled plasma mass spectrometry, e) Polarization loops of KNN and KNN-Na measured under 10 Hz, f) Unipolar strain curves of KNN and KNN-Na measured at 1 Hz.

composition is shown in Table S2. Both samples were non-stoichiometric. The ratio of A-site to B-site ions is lower in KNN (0.96) than in KNN-Na (0.97). Figure 2e shows the hysteresis loops of KNN and KNN-Na. The smaller E_C in KNN-Na can be ascribed to the weak pinning effect due to the fewer A-site vacancies. Figure 2f shows unipolar strain curves of KNN and KNN-Na. The piezoelectric strain coefficient (d_{33}) of KNN and KNN-Na are 240 and 320 pm/V, respectively. The reduction of A-site defects in KNN-Na is responsible for the significant increase in d_{33}. Macroscopic electrical properties can be remarkably affected by intrinsic defects.

Anomalous dielectric behavior (ADB) and defect-driven polarization. Figure 3a, b depict the temperature-dependent dielectric spectra of the two samples. The dielectric properties exhibit an abnormal peak in KNN-Na (around 250 °C) above the orthorhombic-tetragonal (O–T) phase transition temperature, whereas the same peak or ADB is absent in KNN. The dependence of ADB on defect concentration can be revealed by manipulating the latter: KNN-Na is annealed in an oxygen environment at 850 °C for 6 h and aged for 24 h after cooling, as shown in Figure S2a. From Figure 3c, the ADB peak disappeared after annealing. During the oxygen annealing process, defect reactions occur in the material:

$$2V'_A + V_o^{\cdot\cdot} + \frac{1}{2}O_2 \leftrightarrow 2V'_A + O_O^{x} + 2h^{\cdot} \quad (1)$$

$$V_o^{\cdot\cdot} + \frac{1}{2}O_2 + 2e' \leftrightarrow O_O^{x} \quad (2)$$

Heat treatment in air was carried out to eliminate the influence of other factors except oxygen vacancies in the annealing process, as shown in Figure S2a. ADB does not disappear but weakens (Figure S2b). Annealing in air leads to a decrease in oxygen vacancies, which should be correlated with the ADB decrease. The grain size of KNN-Na did not change significantly after O_2 annealing (see Figure S3), suggesting that the change of ADB is caused by the defect concentration rather than the grain size. The permittivity of ferroelectric perovskites is determined by polarization.[9a,25] Due to the kinetics of the polarization process, the polarization relaxations are subject to frequency (see Figure S4). The temperature dependence of dielectric permittivity of KNN-Na was tested at 100 Hz, 1 kHz, 10 kHz, 100 kHz, and 1 MHz, as shown in Figure 3d. It can be found that the permittivity of KNN-Na is significantly affected by frequency in the temperature range of ADB (ADBT). ADB occurs at low frequencies and vanishes at high frequencies (i.e., 100 kHz, 1 MHz). The permittivity of

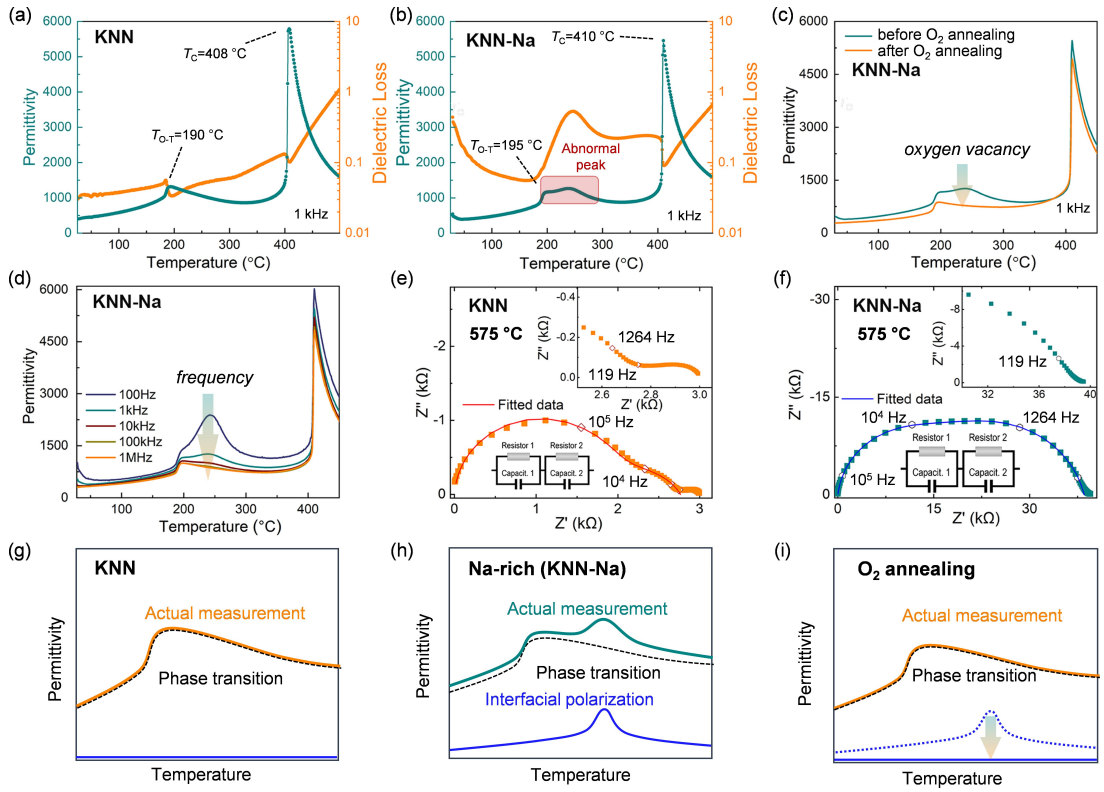

Figure 3. Anomalous dielectric behavior and verification of interfacial polarization. Temperature dependence of dielectric properties for a) KNN and b) KNN-Na. c) Comparison of the temperature dependence of relative permittivity for KNN-Na before and after O_2 annealing. d) Temperature dependence of relative permittivity for KNN-Na in different frequencies. Nyquist plot of e) KNN and f) KNN-Na at 575 °C. Schematics (g), (h), and (i) depicting the individual components constituting the permittivity profile in a) KNN, b) KNN-Na, and c) KNN-Na after the O_2 annealing, respectively.

KNN-Na, corresponding to frequencies of 50 Hz–1 MHz, at the ADB peak temperature (250 °C) and the onset temperature (200 °C) were further studied, as shown in Figure S4. The permittivity of KNN-Na changes significantly at low frequencies, implying the underlying mechanism is interfacial polarization.

The anomalous dielectric peak intensity changes with frequency, i.e., from 100 Hz to 10 kHz. Nyquist plots of the pO_2-dependent impedance of KNN-Na and KNN at 700 °C (Figure 2a and b) readily suggest different electrical responses of KNN-Na compared with KNN. Two semicircles can be seen for KNN-Na, meaning two electrical processes are present, while only one is present for KNN. The second process in KNN-Na most likely resulted from interface polarization. However, the partial pressures used in such experiments are below 0.1 bar. It is, therefore, necessary to use impedance data from measurements in air to compare the second process within a frequency range around ADB.

Such result at 575 °C is depicted in Figure 3e and f, respectively. For both samples, two different semicircles and, thus two resistive responses can be seen. Their respective high to low-frequency arc capacitance values were extracted using two serial R-CPE circuits (R = resistance and CPE = constant phase element) which adequately described the electric and dielectric values (Table S3).[26]

A high-frequency semicircle (4×10^{-10} F) and a low-frequency small semi-circle (1.6×10^{-8} F) can also be detected this time for KNN (Figure 3e). The capacitance value in the range of 10^{-10} F can be attributed to bulk ferroelectric capacitance.[11] The higher capacitance suggests a space charge polarization response. For KNN-Na, the respective high and low-frequency arc capacitance values are 6.5×10^{-10} F and 3.6×10^{-9} F, respectively. The first response can also be attributed to bulk ferroelectric capacitance and is almost identical to KNN. Frequencies of 119 Hz and 1264 Hz, which are annotated in Nyquist plots of KNN-Na (Figure 3f), lie within the second semi-circle response at low frequencies. These frequencies are equivalent to the frequencies in which the ADB is observed in

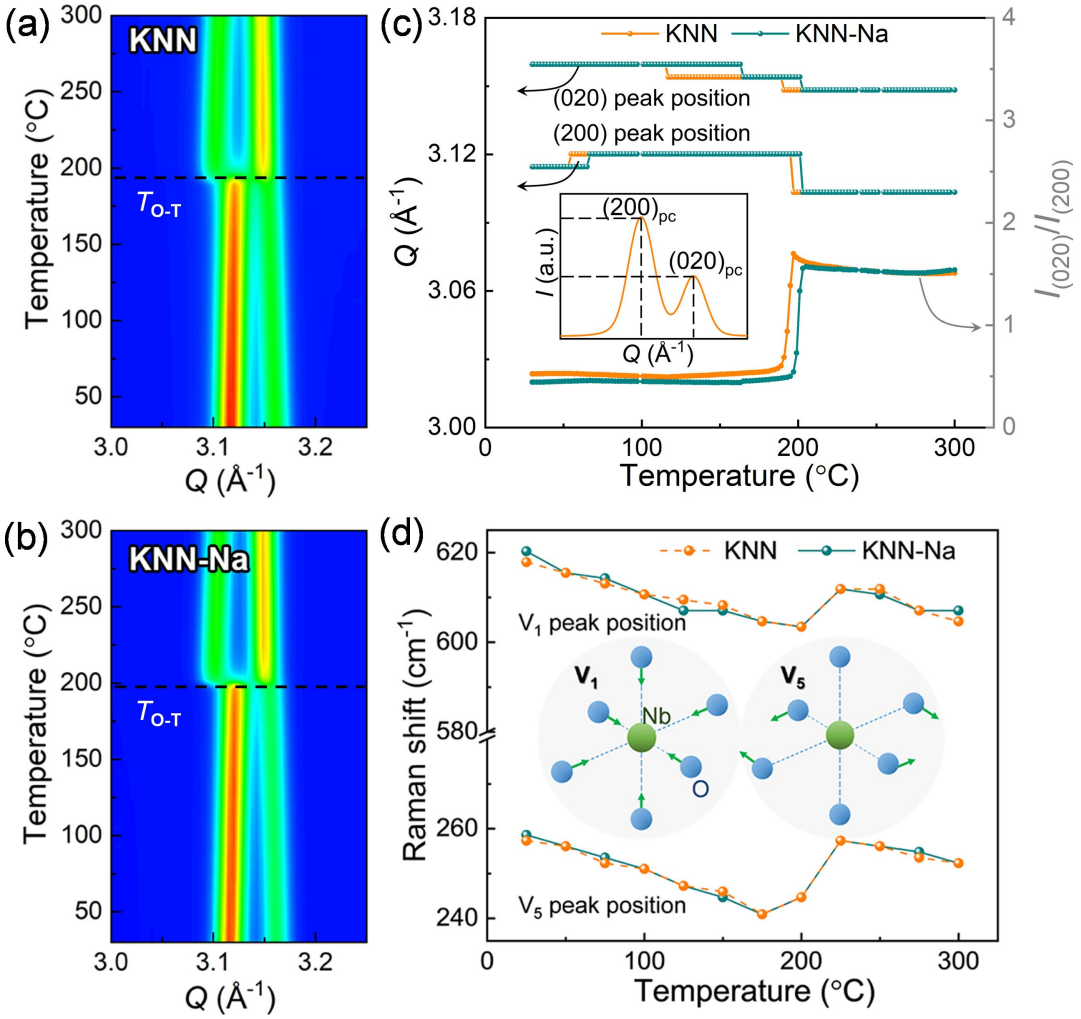

Figure 4. Phase transition. In situ temperature-dependent synchrotron radiation XRD patterns for a) KNN and b) KNN-Na, which were characterized at 2 °C intervals. c) Peak position of (200), (020) in (a), (b) and intensity ratio ($I_{(020)}/I_{(200)}$) from RT to ADBT. d) Raman peak position of V_1, V_5 in KNN, KNN-Na from RT to ADBT. V_1 is stretching mode, and V_5 is bending mode.

KNN-Na (the frequencies of 100 Hz, 1 kHz, and 10 kHz in Figure 3d).

At high frequencies, the space charges cannot follow the change of the field and hence do not induce polarization. This confirms that the 100 kHz and 10 MHz responses in KNN-Na showed no anomalous peak in permittivity (Figure 3d). For the KNN, no ADB can be observed in the whole frequency range, even though there is an interfacial response in this sample. It even has a higher capacitance than the one for KNN-Na. The impact of electrical responses does not only depend on the capacitance but also on the resistance in parallel to it. The resistance of the interface process for the KNN-Na is much higher than for KNN. This puts the transition from the bulk to the interface response right into the range from 100 Hz to 10 kHz. Furthermore, this transition region shifts to higher frequencies in KNN (Figure S5a and S5b). Eventually, this causes the large frequency and temperature-dependent peak, which we call ADB.

We expect that the interfacial polarization is caused by the charge accumulation along the interface in the material under the electric field. To verify this, temperature-dependent *P-E* loops of KNN and KNN-Na were measured, as shown in Figure S6. Below the ADBT region, the ferroelectric properties are hardly affected. However, in the ADBT region, the leakage phenomenon is obvious. The variation of E_C and P_r with temperature is obvious, as shown in Figure S7. This may be caused by the defect that causes the interfacial polarization to move under the high electric field at 10 Hz. Schematics depicting the individual components constituting the permittivity profile, as shown in Figure 3g–i. They correspond to the permittivity near the ADBT region of Figure 3a–c, respectively. There is no interfacial polarization in Figure 3g, and the change of the permittivity is caused by the O–T phase transition. With the reduction of A-site vacancies, there is a response of interfacial polarization in Figure 3h. After the O_2 annealing, the interfacial polarization response disappears, as shown in Figure 3i.

The polarization behavior is also affected by phase structure and chemical bond strength,[25,27] however, these are not the factors causing ADB here. This is shown by investigating the phase structures at different temperatures (from room temperature (RT) to ADB-temperature range

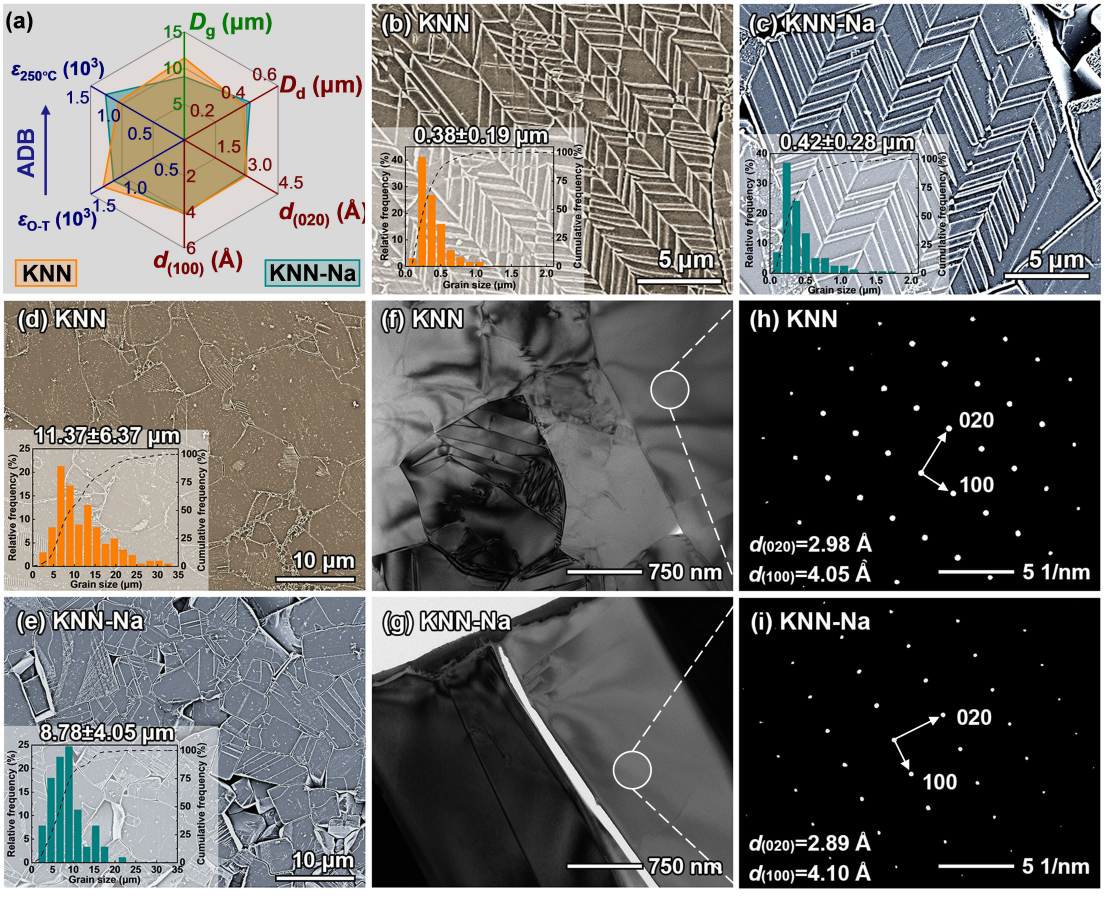

Figure 5. Microstructure comparison. a) Overview of comprehensive properties of KNN and KNN-Na, including relative permittivity at O–T temperature (ε_{O-T}) and 250 °C ($\varepsilon_{250\,°C}$), a distance of grain (D_g) and domain (D_d), an interplanar distance of (100) ($d_{(100)}$) and (020) ($d_{(020)}$). The SEM imagey of the domain of b) KNN and c) KNN-Na. The SEM imagey of the grain of d) KNN and (e) KNN-Na. Domain and grain Size distributions are demonstrated in the insets of (b), (c), (d), and (e) with the average grain sizes marked above. The grain contrast is obtained by chemical corrosion. Grain size can be most realistically reduced. TEM images of (f) KNN and (g) KNN-Na. SAED pattern of (h) KNN and (i) KNN-Na.

(ADBT)), as seen in Figure 4a–c, and Figure S8. It can be noted that both samples possess the pure perovskite structure.[27] Figure 4d compares the chemical vibration modes at different temperatures (from RT to ADBT) for the two samples. Besides, it can be found that the peak positions of V1 and V5 vibrations of the two samples are identical (see Figure S9 and S10) indicating that the chemical bond and atomic vibrations of the two have no significant difference.[28]

Figure 5a–c, show that the domain sizes of KNN and KNN-Na are similar. As shown in Figure 5a, d, e, and Figure S3, the effect of grain sizes on the ADB is limited. In addition, the morphologies of the shape of domains inside the grains of the two samples are similar (regular herring-bone-like ferroelectric domains), in agreement with the TEM results shown in Figure 5f and g. The interplanar spacing (100) of KNN-Na in the selected area electron diffraction (SAED) is slightly larger than that of KNN, while (020) is smaller than KNN, as shown in Figure 5a, h and f, implying that the excess Na suppressed the A-site vacancies and causes weak lattice distortion. Therefore, the ADB observed in KNN-Na can be exclusively related to the defect-driven interfacial polarization.

Conclusion

A new frame for analyzing defects was derived from defect chemistry calculations. By measuring electrical conductivity and oxygen partial pressure, the defect concentration in perovskite oxides can be semi-quantitatively analyzed. This approach is applicable for A-site defects that are hard to study by other measurement methods. An in-depth study of the polarization mechanism in potassium sodium niobate was performed, showing that the interfacial polarization indeed resulted from the defect accumulations. This approach can also be used for other perovskite oxide systems, which can potentially improve our understanding on defects in such systems and benefit functional ferroelectric perovskite design.

Acknowledgements

This work was supported by the National Key Research and Development Program of China (No. 2020YFA0711700, 2020YFA0710401), the National Nature Science Foundation of China (Grant 52032005), the Beijing Natural Science Foundation (No. JQ20009), and the German Research Foundation (DFG 419400593). The BL02U2 beamline of SSRF is acknowledged for the provision of experimental beamtime. Open Access funding enabled and organized by Projekt DEAL.

Conflict of Interest

The authors declare no conflict of interest.

Data Availability Statement

The data that support the findings of this study are available from the corresponding author upon reasonable request.

Keywords: A-Site Defect · Defect Engineering · Interfacial Polarization · Oxygen Partial Pressure · Perovskites

[1] H. J. Snaith, *Nat. Mater.* **2018**, *17*, 372–376.
[2] G. Long, R. Sabatini, M. I. Saidaminov, G. Lakhwani, A. Rasmita, X. Liu, E. H. Sargent, W. Gao, *Nat. Rev. Mater.* **2020**, *5*, 423–439.
[3] R. E. Cohen, *Nature* **1992**, *358*, 136–138.
[4] a) J. W. Lee, S. Tan, S. I. Seok, Y. Yang, N. G. Park, *Science* **2022**, *375*, eabj1186; b) J. Kang, J. Li, S. H. Wei, *Appl. Phys. Rev.* **2021**, *8*, 031302; c) J. M. Ball, A. Petrozza, *Nat. Energy* **2016**, *1*, 16149; d) L. K. Ono, S. Liu, Y. Qi, *Angew. Chem. Int. Ed.* **2020**, *59*, 6676–6698; *Angew. Chem.* **2020**, *132*, 6740–6764.
[5] a) N. Nuraje, K. Su, *Nanoscale* **2013**, *5*, 8752–8780; b) G. F. Nataf, M. Guennou, J. M. Gregg, D. Meier, J. Hlinka, E. K. H. Salje, J. Kreisel, *Nat. Rev. Phys.* **2020**, *2*, 634–648.
[6] a) N. J. Donnelly, C. A. Randall, *IEEE Trans. Ultrason. Ferroelectr. Freq. Control* **2012**, *59*, 1883–1887; b) T. Rojac, S. Drnovsek, A. Bencan, B. Malic, D. Damjanovic, *Phys. Rev. B* **2016**, *93*, 014102; c) T. N. Nguyen, H. C. Thong, Z. X. Zhu, J. K. Nie, Y. X. Liu, Z. Xu, P. S. Soon, W. Gong, K. Wang, *J. Mater. Res.* **2021**, *36*, 996–1014.
[7] a) H. Liu, H. Wu, K. P. Ong, T. Yang, P. Yang, P. K. Das, X. Chi, Y. Zhang, C. Diao, W. K. A. Wong, E. P. Chew, Y. F. Chen, C. K. I. Tan, A. Rusydi, M. B. H. Breese, D. J. Singh, L. Q. Chen, S. J. Pennycook, K. Yao, *Science* **2020**, *369*, 292–297; b) H. Wu, S. Ning, M. Waqar, H. Liu, Y. Zhang, H. H. Wu, N. Li, Y. Wu, K. Yao, T. Lookman, X. Ding, J. Sun, J. Wang, S. J. Pennycook, *Nat. Commun.* **2021**, *12*, 2841; c) M. Waqar, H. Wu, K. P. Ong, H. Liu, C. Li, P. Yang, W. Zang, W. H. Liew, C. Diao, S. Xi, D. J. Singh, Q. He, K. Yao, S. J. Pennycook, J. Wang, *Nat. Commun.* **2022**, *13*, 3922.
[8] H. Liu, Y.-X. Liu, A. Song, Q. Li, Y. Yin, F.-Z. Yao, K. Wang, W. Gong, B.-P. Zhang, J.-F. Li, *Natl. Sci. Rev.* **2022**, *9*, nwac101.
[9] a) M. N. Rahaman, Ceramic Processing and Sintering; CRC press: Boca Raton, **2017**; b) F. Yang, H. Zhang, L. Li, I. M. Reaney, D. C. Sinclair, *Chem. Mater.* **2016**, *28*, 5269–5273.
[10] I. P. Bykov, Y. A. Zagorodniy, L. P. Yurchenko, A. M. Korduban, K. Nejezchleb, V. V. Trachevsky, V. Dimza, L. Jastrabik, A. Dejneka, *IEEE Trans. Ultrason. Ferroelectr. Freq. Control* **2014**, *61*, 1379–1385.
[11] M. Guan, C. Xiao, J. Zhang, S. Fan, R. An, Q. Cheng, J. Xie, M. Zhou, B. Ye, Y. Xie, *J. Am. Chem. Soc.* **2013**, *135*, 10411–10417.
[12] a) J. T. S. Irvine, D. C. Sinclair, A. R. West, *Adv. Mater.* **1990**, *2*, 132–138; b) M. Li, M. J. Pietrowski, R. A. De Souza, H. Zhang, I. M. Reaney, S. N. Cook, J. A. Kilner, D. C. Sinclair, *Nat. Mater.* **2014**, *13*, 31–35.
[13] Y. Jiang, C. Qin, M. Cui, T. He, K. Liu, Y. Huang, M. Luo, L. Zhang, H. Xu, S. Li, J. Wei, Z. Liu, H. Wang, G. H. Kim, M. Yuan, J. Chen, *Nat. Commun.* **2019**, *10*, 1868.
[14] a) H. Liu, P. Veber, J. Rödel, D. Rytz, P. B. Fabritchnyi, M. I. Afanasov, E. A. Patterson, T. Frömling, M. Maglione, J. Koruza, *Acta Mater.* **2018**, *148*, 499–507; b) Z.-T. Li, H. Liu, H.-C. Thong, Z. Xu, M.-H. Zhang, J. Yin, J.-F. Li, K. Wang, J. Chen, *Adv. Electron. Mater.* **2019**, *5*, 1800756.
[15] T. Rojac, A. Bencan, G. Drazic, N. Sakamoto, H. Ursic, B. Jancar, G. Tavcar, M. Makarovic, J. Walker, B. Malic, D. Damjanovic, *Nat. Mater.* **2017**, *16*, 322–327.

[16] V. J. Keast, *Mater. Charact.* **2012**, *73*, 1–7.
[17] H. Sha, J. Cui, R. Yu, *Sci. Adv.* **2022**, *8*, eabn2275.
[18] L. Eyraud, B. Guiffard, L. Lebrun, D. Guyomar, *Ferroelectrics* **2006**, *330*, 51–60.
[19] S. Kong, N. Kumar, S. Checchia, C. Cazorla, J. Daniels, *Adv. Funct. Mater.* **2019**, *29*, 1900344.
[20] a) K. Wang, J. F. Li, *Adv. Funct. Mater.* **2010**, *20*, 1924–1929; b) Y. X. Liu, H. C. Thong, Y. Y. S. Cheng, J. W. Li, K. Wang, *J. Appl. Phys.* **2021**, *129*, 024102.
[21] a) L. Koch, S. Steiner, K.-C. Meyer, I.-T. Seo, K. Albe, T. Frömling, *J. Mater. Chem. C* **2017**, *5*, 8958–8965; b) F. Yang, Y. Hu, Q. Hu, S. Steiner, T. Frömling, L. Li, P. Wu, E. Pradal-Velázquez, D. C. Sinclair, *J. Mater. Chem. A* **2022**, *10*, 891–901.
[22] a) M. H. Zhang, K. Wang, Y. J. Du, G. Dai, W. Sun, G. Li, D. Hu, H. C. Thong, C. Zhao, X. Q. Xi, Z. X. Yue, J. F. Li, *J. Am. Chem. Soc.* **2017**, *139*, 3889–3895; b) H. Tao, H. Wu, Y. Liu, Y. Zhang, J. Wu, F. Li, X. Lyu, C. Zhao, D. Xiao, J. Zhu, S. J. Pennycook, *J. Am. Chem. Soc.* **2019**, *141*, 13987–13994; c) H.-C. Thong, C. Zhao, Z. Zhou, C.-F. Wu, Y.-X. Liu, Z.-Z. Du, J.-F. Li, W. Gong, K. Wang, *Mater. Today* **2019**, *29*, 37–48; d) Y. Saito, H. Takao, T. Tani, T. Nonoyama, K. Takatori, T. Homma, T. Nagaya, M. Nakamura, *Nature* **2004**, *432*, 84–87; e) J. Wu, D. Xiao, J. Zhu, *Chem. Rev.* **2015**, *115*, 2559–2595.
[23] a) S. Fop, J. M. Skakle, A. C. McLaughlin, P. A. Connor, J. T. Irvine, R. I. Smith, E. J. Wildman, *J. Am. Chem. Soc.* **2016**, *138*, 16764–16769; b) C. Long, Q. Chang, H. Fan, *Sci. Rep.* **2017**, *7*, 4193.
[24] S. Aggarwal, R. Ramesh, *Annu. Rev. Mater. Sci.* **1998**, *28*, 463–499.
[25] Y. Yao, C. Zhou, D. Lv, D. Wang, H. Wu, Y. Yang, X. Ren, *EPL-Europhys. Lett.* **2012**, *98*, 27008.
[26] E. Barsoukov, J. R. Macdonald, Impedance Spectroscopy Theory, Experiment, and Applications; John Wiley & Sons, Inc., Hoboken, **2005**.
[27] L. E. Cross, *Ferroelectrics* **1994**, *151*, 305–320.
[28] L. P. Xu, K. Jiang, J. Z. Zhang, G. S. Xu, Z. G. Hu, J. H. Chu, *Appl. Phys. Lett.* **2015**, *106*, 122901.

Manuscript received: November 15, 2022
Accepted manuscript online: December 16, 2022
Version of record online: January 19, 2023